PNAS RESEARCH ARTICLE | SUSTAINABILITY SCIENCE

Charting C–C coupling pathways in electrochemical CO_2 reduction on Cu(111) using embedded correlated wavefunction theory

Qing Zhao[a], John Mark P. Martirez[b], and Emily A. Carter[a,b,c,1]

Contributed by Emily Carter; received February 17, 2022; accepted September 28, 2022; reviewed by Marc Koper and Aravind Asthagiri

The electrochemical CO_2 reduction reaction (CO_2RR) powered by excess zero-carbon-emission electricity to produce especially multicarbon (C_{2+}) products could contribute to a carbon-neutral to carbon-negative economy. Foundational to the rational design of efficient, selective CO_2RR electrocatalysts is mechanistic analysis of the best metal catalyst thus far identified, namely, copper (Cu), via quantum mechanical computations to complement experiments. Here, we apply embedded correlated wavefunction (ECW) theory, which regionally corrects the electron exchange-correlation error in density functional theory (DFT) approximations, to examine multiple C–C coupling steps involving adsorbed CO (*CO) and its hydrogenated derivatives on the most ubiquitous facet, Cu(111). We predict that two adsorbed hydrogenated CO species, either *COH or *CHO, are necessary precursors for C–C bond formation. The three kinetically feasible pathways involving these species yield all three possible products: *COH–CHO, *COH–*COH, and *OCH–*OCH. The most kinetically favorable path forms *COH–CHO. In contrast, standard DFT approximations arrive at qualitatively different conclusions, namely, that only *CO and *COH will prevail on the surface and their C–C coupling paths produce only *COH–*COH and *CO–*CO, with a preference for the first product. This work demonstrates the importance of applying qualitatively and quantitatively accurate quantum mechanical method to simulate electrochemistry in order ultimately to shed light on ways to enhance selectivity toward C_{2+} product formation via CO_2RR electrocatalysts.

electrocatalysis | carbon dioxide | electroreduction | copper | carbon–carbon coupling

Significance

Electrochemical CO_2 reduction (CO_2R) offers the dual promise of recycling the most prevalent greenhouse gas while producing valuable products without resorting to further petroleum extraction. The lack of efficient electrocatalysts impedes its further development. Rational design of CO_2R electrocatalysts with superior activity and selectivity must begin with understanding the mechanism on the best existing catalyst, copper (Cu). Using embedded correlated wavefunction theory, we find that adsorbed (*) hydrogenated carbon monoxide in either isomeric form, *COH and *CHO, precedes C–C coupling toward multicarbon products on Cu(111), forming *COH–CHO, *COH–*COH, and *OCH–*OCH, with *COH–CHO most favorable, which prior studies heretofore overlooked. This study inspires design principles for CO_2R electrocatalysts with enhanced activity and selectivity toward multicarbon hydrocarbons.

The electrochemical CO_2 reduction reaction (CO_2RR) represents one promising solution to achieve a carbon-neutral cycle by using excess renewable electricity to produce fuels and chemicals (1–3). In particular, C_{2+} products with high energy density are more attractive than methane and H_2 as fuels and feedstock for chemical industries (4). Copper (Cu)-based materials remain the only electrocatalysts for CO_2RR to produce valuable hydrocarbon products that go beyond two-electron reduction, forming higher hydrocarbons than carbon monoxide or formic acid (5–9).

The major C_2 products of Cu-catalyzed CO_2R are ethylene and ethanol, along with other minor products (glycolaldehyde, acetic acid, acetaldehyde, and ethylene glycol) (10). However, Cu requires high overpotentials to achieve reasonable reaction rates, and it exhibits poor selectivity toward the above-mentioned C_2 products, limiting its practical applications (3, 7, 10, 11). To discover and design better CO_2RR electrocatalysts, many experimentalists have tried to detect reaction intermediates and to propose reaction mechanisms leading to C–C coupling on Cu. For example, Pérez-Gallent et al. observed with in situ Fourier transform infrared spectroscopy a hydrogenated dimer intermediate, *CO–*COH (asterisk means adsorbed, and the element symbol next to the asterisk is the type of atom directly bound to the surface), on Cu(100) but not on Cu(111) (12). Electrochemical mass spectrometry measurements of CO reduction on two Cu facets led Schouten et al. to propose two distinct pathways for ethylene formation on Cu(111) and Cu(100) (11, 13). One nonselective path on both facets involves an intermediate that yields both methane and ethylene. The other path selective toward ethylene was suggested to occur on Cu(100) alone (11, 13). Specifically for the latter path, they proposed that CO dimer is a key intermediate on Cu(100), based on two observations: 1) this facet exhibits selective reduction of CO to ethylene, not methane, at relatively low overpotentials, indicating that C–C bonds might form very early in a separate pathway from methane production and 2) ethylene formation on Cu(100) is pH independent, suggesting that the pathway does not involve protons in or before the rate-limiting step of C–C coupling (11, 14). In other work, Bertheussen et al. proposed acetaldehyde as a key intermediate in ethanol formation on oxide-derived Cu

Author contributions: E.A.C. designed research; Q.Z. performed research; E.A.C. guided research; Q.Z., J.M.P.M., and E.A.C. analyzed data; and Q.Z., J.M.P.M., and E.A.C. wrote the paper.

Reviewers: A.A., The Ohio State University; and M.K., Universiteit Leiden.

The authors declare no competing interest.

[1] To whom correspondence may be addressed. Email: eac@princeton.edu.

This article contains supporting information online at http://www.pnas.org/lookup/suppl/doi:10.1073/pnas.2202931119/-/DCSupplemental.

electrodes, based on NMR spectroscopy and static headspace gas chromatography analysis of the liquid-phase products of CO reduction (15). Despite these important studies, experimental identification of all reaction intermediates and the associated pathways involved in the CO_2RR remains a significant challenge due to the fleeting nature of intermediates and the lack of in operando surface probes.

Alternatively, periodic density functional theory (DFT) investigations have helped assess various C–C coupling pathways and at times mapped out entire reaction mechanisms yielding C_2 products on Cu surfaces. For example, Luo et al. examined different C–C coupling routes using DFT with the Perdew–Burke–Ernzerhof (PBE) (16) exchange-correlation (XC) functional (DFT-PBE), concluding that ethylene forms via coupling of two *CHO species on Cu(100) (17). However, Garza et al. predicted that coupling on Cu(100) occurs through a *CO–CHO pathway, based on DFT with the revised PBE XC functional of Hammer et al. (RPBE) (18) and a constant electrode potential model (19). They proposed full mechanisms forming seven possible unique C_2 products including ethylene and ethanol (19). Calle-Vallejo et al. used DFT-PBE to propose instead that C–C coupling on Cu(100) occurs via *CO dimerization, followed by a proton-coupled electron transfer (PCET) step to form *CO–*COH (20). Cheng et al. offered further support for this pathway by performing DFT-PBE molecular dynamics simulations with a full description of explicit solvent in contact with Cu(100) (21). Liu et al. subsequently proposed this latter mechanism for stepped Cu(211) based on DFT using a Bayesian error estimation XC functional with a van der Waals correction (BEEF-vdW) (22, 23). Xiao et al. considered the CO_2RR pH dependence on Cu(111) using DFT-PBE, predicting that C–C coupling occurs via a *CO–*COH pathway at neutral pH, with *CO dimerization dominating at high pH (24). Related progress (25) has been reported in simulating constant potential conditions for CO dimerization at the Cu(100)–water interface (26), along with understanding more generally how pH (27) and electric field (28) influence electrocatalysis.

All of the above-mentioned prior theoretical studies were conducted using DFT with generalized-gradient approximations (GGAs), which incorrectly predict the CO adsorption site (adsite) on Cu surfaces (29, 30) and improperly describe electron transfer (31–33). In contrast, Sharifzadeh et al. reproduced the experimentally observed CO adsite (atop) and the measured binding energy for atop-site adsorption of CO on Cu(111) [0.49 eV vs. experimental measurements of 0.45 to 0.52 eV (34–37)] using embedded correlated wavefunction (ECW) theory (38–42), which correctly predicts the π-backbonding interaction between CO and Cu surfaces (43). We recently further validated the accuracy of ECW theory (38–42) against experiments, by demonstrating its ability to describe properly the observed potential-dependent kinetics of the CO_2RR on Cu(111) (44, 45). By contrast, van der Waals–corrected standard DFT-GGA fails to reproduce the experimental kinetics (44, 45). These findings motivated the present work to use ECW theory to reexamine C–C coupling steps on Cu surfaces, as a next refinement in unraveling the CO_2RR mechanism for producing higher hydrocarbons such as ethylene. ECW theory predicts that *CO reduces almost equally easily to either *COH or *CHO on Cu(111) at experimental onset potentials, whereas the majority of DFT-GGA simulations predict that only *COH should form, a qualitatively different conclusion (44, 45). This suggests the existence of more possible C–C coupling pathways on this surface than previously investigated (Fig. 1).

Here we study all seven possible C–C bond formation pathways on Cu(111) using ECW theory. Elucidating C–C coupling mechanisms on this most stable facet, among others, is crucial since polycrystalline Cu electrodes, not single-crystal Cu electrodes, are more likely to be used in practice. Recent electron backscatter diffraction experiments characterized a polycrystalline Cu electrode's surface to be a combination of primarily Cu(111), (100), and (110) facets, with these three exhibiting comparable cathodic current densities (measured via high-resolution scanning electrochemical cell microscopy); thus, the overall CO_2R activity of polycrystalline Cu electrodes reflects such facet diversity (46), and the mechanisms on multiple facets, including Cu(111), are therefore of interest. Furthermore, the activity and selectivity of the Cu(111) facet toward generation of multicarbon products can be enhanced greatly by introducing defects (47), microstructures (48), and dopants in the surface (49) and incorporating large monovalent cations, e.g., Cs^+, in the electrolyte (50). Overall, a qualitatively and quantitatively reliable mechanistic analysis of C–C coupling on Cu(111) provides a foundational benchmark for comparing to other facets and for understanding the C–C coupling–promoting effects of compositional and structural modifications of this facet.

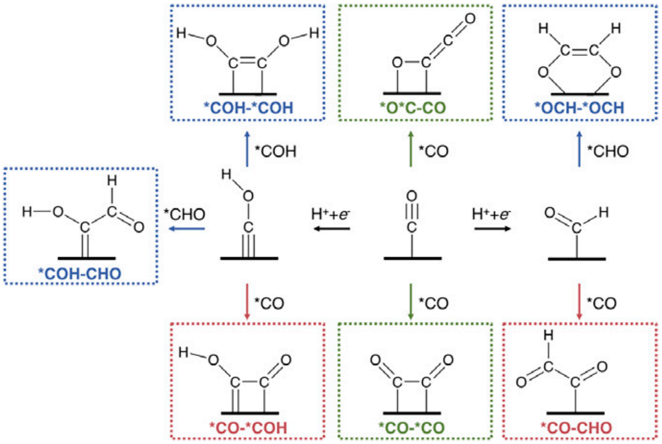

Fig. 1. Possible reaction pathways considered for C–C coupling in electrochemical CO_2R toward C_{2+} products on Cu(111). The green paths denote coupling of two *CO (*O*C–CO and *CO–*CO), the red paths represent coupling of a *CO and a hydrogenated *CO (*CO–*COH and *CO–CHO), and the blue paths represent coupling of two hydrogenated *CO (*COH–CHO, *COH–*COH, and *OCH–*OCH).

Computational Methods

ECW theory offers a regional correction to DFT calculations to obtain an improved description of electron XC. We therefore describe here the periodic DFT details first, followed by details of the ECW computations.

Periodic DFT Calculations. We performed spin-polarized periodic DFT calculations using the Vienna Ab initio Simulation Package (VASP) (51, 52) version 5.4.4 with the PBE (16) XC functional and Grimme's D3 dispersion correction (53, 54) with the Becke-Johnson damping function (55) (DFT-PBE-D3). We used Blöchl's all-electron, frozen-core, projector augmented-wave (PAW) (56) method, with the standard PAW projectors in VASP (57, 58) to describe the valence electron–ion (screened nucleus) interactions. The self-consistently optimized valence-electron wavefunctions included the 1*s* electron of H, the 2*s* and 2*p* electrons of C and O, and the 4*s* and 3*d* electrons of Cu. We imposed a kinetic energy cutoff of 660 eV for the plane wave (PW) basis set. We employed a five-layer, 4 × 4 supercell (80 Cu atoms) to represent a Cu(111) surface and to determine the adsites and reaction pathways of *O*C–CO, *CO–*COH, *CO–CHO, *COH–CHO, *COH–*COH, and *OCH–*OCH. A larger, five-layer, 5 × 5 supercell (125 Cu atoms) was used for determining the *CO–*CO adsite and reaction pathway due to the inclusion of two explicit water molecules (vide infra). We sampled the Brillouin zone using 4 × 4 × 1 and 3 × 3 × 1 Γ-point–shifted Monkhorst–Pack (59) *k*-point grids for the 4 × 4 and 5 × 5 slabs, respectively, consistent with our previous study (45). Methfessel–Paxton (60) electronic smearing with a smearing width of 0.09 eV aided self-consistent field convergence. We added at least 15 Å of vacuum along surface normal to avoid interactions between periodic images. We relaxed the Cu atoms in the three topmost layers and fixed the Cu atoms in the two bottommost layers at their bulk atomic positions to simulate a semiinfinite surface. We placed the adsorbates and explicit water molecules on one side of the surface, and thus, we applied dipole field energy and potential corrections (61) to cancel the artificial field interactions imposed by the periodic boundary conditions. We structurally relaxed the atoms until the maximum absolute atomic force was smaller than 0.03 eV/Å during geometry optimizations.

We determined the minimum energy paths (MEPs) for C–C coupling steps using the climbing image nudged elastic band (CI-NEB) (62) method with an artificial spring force constant of 3 eV/Å^2 along the reaction tangents. Fig. 2 *A–G* shows the critical structures along the MEPs for C–C coupling steps (the full sets of geometries are in *SI Appendix*, Figs. S1–S7). We added two explicit water molecules to stabilize the *CO–*CO intermediate on Cu(111) (details are in *Results and Discussion*). To further understand explicit solvation effects, we also tested the influence of including one or two explicit water molecules on DFT-PBE-D3 barriers for all other C–C coupling pathways (vide infra). We did not consider the effect of implicit continuum solvation (63, 64) in this work because the stationary states and intermediates of C–C coupling reactions are charge-neutral (unlike in PCET reactions where we routinely include not just implicit continuum solvation but also explicit water molecules). We therefore expect long-range solvation effects to cancel out along the MEPs for these C–C coupling reactions. We converted the electronic energies to Gibbs free energies by including zero-point energies, thermal corrections, and entropy terms (at 298.15 K) using the harmonic oscillator approximation. In the vibrational frequency calculations, we included the contributions from all adsorbates, water molecules, and all topmost layer Cu atoms.

ECW Calculations. Within ECW theory (38–42), one partitions the total system (i.e., the periodic slab in this work) into two subsystems: the cluster on which the reaction occurs and its environment, consisting of the remainder of the total system. To recover the interaction between the cluster and its environment, we use an embedding potential, V_{emb}, optimized with density functional embedding theory (39, 41, 42). The final ECW energy is defined as

$$E_{\mathrm{ECW}} = E_{\mathrm{slab}}^{\mathrm{DFT-PW}} + (E_{\mathrm{emb-cluster}}^{\mathrm{CW}} - E_{\mathrm{emb-cluster}}^{\mathrm{DFT}}).$$

$E_{\mathrm{slab}}^{\mathrm{DFT-PW}}$ is the PW DFT energy of the periodic slab (we remove the D3 dispersion correction to avoid double counting since our correlated wavefunction (CW) calculations formally contain the dispersion energy, vide infra). $E_{\mathrm{emb-cluster}}^{\mathrm{CW}}$ and $E_{\mathrm{emb-cluster}}^{\mathrm{DFT}}$ are the energies of the embedded cluster from CW and DFT methods in the presence of the embedding potential, V_{emb}. In this way, the self-interaction and delocalization errors inherent in the periodic PW-DFT calculations arising from XC approximations can be regionally corrected. The corrections performed on the embedded cluster, which contains the catalytically active sites, achieve this effect. This framework extends the application of computationally demanding CW methods from small or medium-sized molecules to heterogeneous catalysis, which is otherwise intractable.

In this work, we considered four different clusters (Fig. 2 *A–G*) to represent the important catalytic sites. We chose the clusters based on the geometries of the adsorbates along the MEPs. We ensure all adsorbates and explicit water molecules reside within the cluster region and do not extend into the environment and thus do not overlap the embedding potential region. The embedding potential is meant to be a boundary condition and therefore should not directly interact with the adsorbates or solvent molecules. Rather, it interacts with the metal cluster to reproduce the electronic behavior of an extended metal surface facet by reproducing the original electron density distribution of the extended metal surface. In addition, we always use an even number of total electrons in the adsorbates-cluster model system to avoid introducing artificial spin polarization (due to what would be a spurious unpaired electron) in the embedded cluster calculations. We selected a Cu_{16} cluster for the *CO–*CO adsite and path; a Cu_{10} cluster for *O*C–CO, *COH–*COH, *OCH–*OCH, and *COH–CHO adsites and *O*C–CO path; a Cu_{11} cluster for *CO–*COH and *CO–CHO adsites and paths; and a Cu_{12} cluster for *COH–*COH, *OCH–*OCH, and *COH–CHO paths. In some cases, we used a larger cluster for paths than for adsites, specifically, Cu_{12} vs. Cu_{10} for *COH–*COH, *OCH–*OCH, and *COH–CHO. This was done to ensure that all structural intermediates along a pathway, and not only the product, reside within the cluster region. This systematic approach to cluster size selection was validated in earlier work (44, 45, 65).

We carved out these clusters from a four-layer 5 × 5 Cu slab (100 Cu atoms) representing the total system and then solved for the embedding potentials, V_{emb}, for each of these clusters (without adsorbates) using optimized effective potential theory at the periodic PW-DFT-PBE level using an in-house modified VASP code version 5.3.3, by maximizing the extended Wu–Yang functional (66):

$$W[V_{\mathrm{emb}}] = E_{\mathrm{cluster}}[\rho_{\mathrm{cluster}}, V_{\mathrm{emb}}] + E_{\mathrm{env}}[\rho_{\mathrm{env}}, V_{\mathrm{emb}}] - \int V_{\mathrm{emb}}\rho_{\mathrm{tot}}\mathrm{d}r.$$

E_{cluster} and E_{env} are the self-consistently optimized DFT energies of the cluster and its environment in the presence of V_{emb}, respectively. ρ_{cluster} and ρ_{env} are the corresponding cluster and environment self-consistently optimized electron densities in the presence of V_{emb}, respectively. The last term is the interaction between the periodic slab DFT electron density, ρ_{tot}, and V_{emb}. Maximizing the extended Wu–Yang functional with respect to variations in V_{emb} yields

$$\rho_{\mathrm{cluster}} + \rho_{\mathrm{env}} = \rho_{\mathrm{tot}},$$

indicating electron density recovery of the total system (i.e., summation of embedded subsystem electron densities equals the electron density of the total system) at the DFT level, which is the metric for convergence of the embedding potential.

Once we obtain the optimized embedding potential (Fig. 2 *H–K*), we compute the two terms of embedded cluster energies, $E_{\mathrm{emb-cluster}}^{\mathrm{CW}}$ and $E_{\mathrm{emb-cluster}}^{\mathrm{DFT}}$, in the final ECW energy expression, which employs V_{emb} as a one-electron operator in the CW Hamiltonian. We performed embedded cluster calculations in MOLPRO (67, 68) version 2012.1 with Gaussian-type orbital (GTO) basis sets. The basis sets used were all-electron correlation-consistent polarized valence double zeta (cc-pVDZ) (69) bases for C, H, and O, and the Los Alamos National Laboratory 2-double-zeta (LANL2DZ) (70) basis for the 19 outermost electrons of Cu,

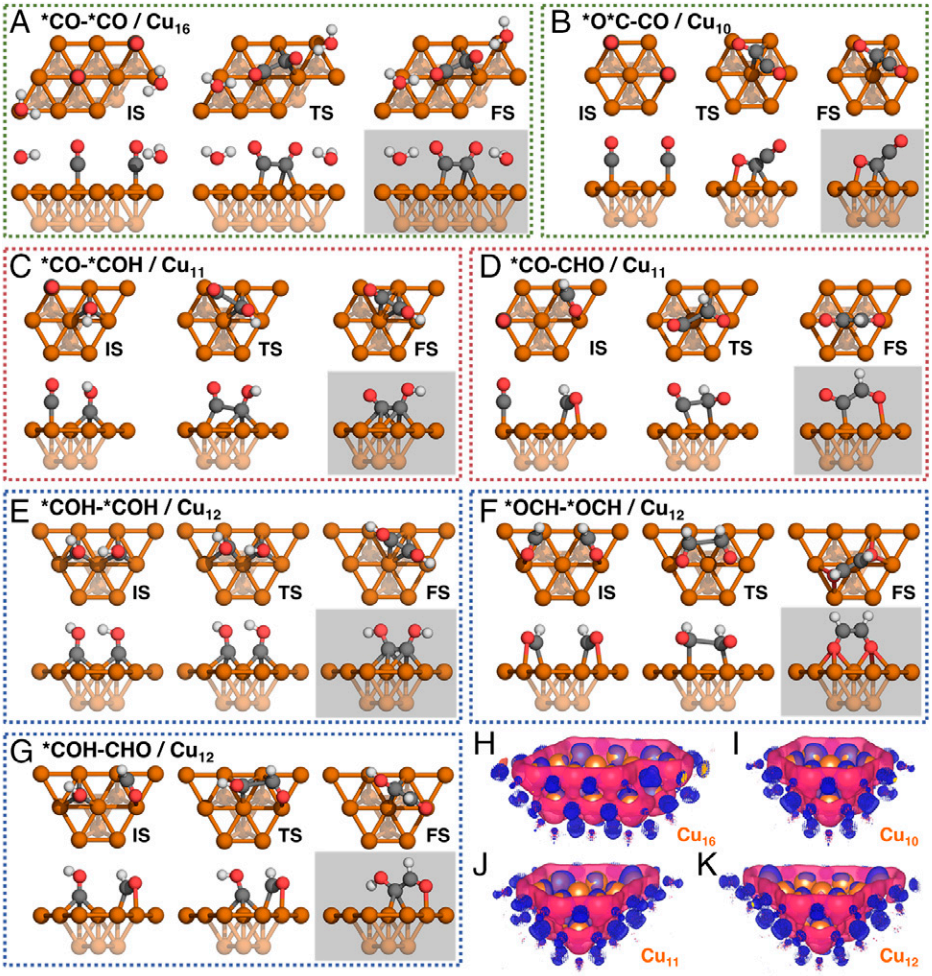

Fig. 2. Initial state (IS), transition state (TS), and FS structures ([*Top*] top and [*Bottom*] side views) optimized within DFT-PBE-D3 along the MEPs starting from ECW-predicted preferred adsite structures for reactants and products in C–C coupling steps to form (*A*) *CO–*CO, (*B*) *O*C–CO, (*C*) *CO–*COH, (*D*) *CO–CHO, (*E*) *COH–*COH, (*F*) *OCH–*OCH, and (*G*) *COH–CHO on Cu(111). Here only *A* has two explicit solvating water molecules, although explicit solvation tests have been done for all of these paths within DFT-PBE-D3 (vide infra). Atoms are colored as follows: Cu in brown (subsurface atoms are faded out), C in dark gray, O in red, and H in light gray. Only the Cu cluster fragments used in the ECW pathway calculations of the slabs are shown. Isosurface plots (blue, +1 V; magenta, −1 V) of the embedding potentials generated for (*H*) the Cu_{16} cluster and its Cu_{84} environment for *CO–*CO adsites and path; (*I*) the Cu_{10} cluster and its Cu_{90} environment for *O*C–CO, *COH–*COH, *OCH–*OCH, and *COH–CHO adsites and the *O*C–CO path; (*J*) the Cu_{11} cluster and its Cu_{89} environment for *CO–*COH and *CO–CHO adsites and paths; and (*K*) the Cu_{12} cluster and its Cu_{88} environment for the *COH–*COH, *OCH–*OCH, and *COH–CHO paths.

with the corresponding LANL2DZ effective core potential (ECP) representing the 10 innermost core electrons. For the embedded cluster calculations, we modify the original one-electron Hamiltonian (h^0) as $h^0 + V_{\mathrm{emb}}$ to include the interactions between the cluster and its environment represented in the atomic orbital (AO) basis. The matrix operation feature in MOLPRO facilitates this modification. To generate the embedding integral matrices, $\langle \mathrm{AO}|V_{\mathrm{emb}}|\mathrm{AO}\rangle$, we use our standalone embedding code, EmbeddingIntegralGenerator (71), which is available on GitHub.

We construct the molecular geometries for embedded cluster calculations by adding the adsorbates (and explicit water molecules when applicable) onto the bare embedded clusters. We fix the adsorbates at their periodic PW-DFT–optimized structures along the MEPs. We use the same embedding potential for a given cluster size and geometry for all adsorbate geometries along an MEP to avoid potential numerical inconsistencies in the energy surface and to save computation time by not reoptimizing the embedding potential for each adsorbate geometry along the MEP. Again, as the embedding potential is meant to be a relatively far-field boundary condition, then as long as the reaction is contained within the cluster region, it makes physical sense to keep the embedding potential fixed along a reaction path, representing the interaction of the metal cluster with its extended metallic environment. Given the very short-range screening length of metals (typically a metal–metal bond length), this fixed embedding potential approximation works well.

We computed $E^{\mathrm{DFT}}_{\mathrm{emb-cluster}}$ using embedded spin-polarized GTO DFT-PBE, whereas we calculated $E^{\mathrm{CW}}_{\mathrm{emb-cluster}}$ via embedded complete active space second-order perturbation theory (72, 73) (emb-CASPT2). The emb-CASPT2 calculations utilized reference wavefunctions generated from embedded complete active space self-consistent field theory (74, 75) (emb-CASSCF). The ECW work begins by screening a large number of possible adsites at the ECW level for each intermediate to determine adsite preference. We first established appropriate active spaces (ASs) in emb-CASSCF for this screening step, followed by determining appropriate ASs for reaction pathways. *SI Appendix*, Figs. S8–S14 and S15–S21 display the self-consistently optimized natural orbitals of the ASs for screening adsites and studying paths, respectively.

The AS for screening *CO–*CO adsites consisted of (12e, 12o), i.e., 12 electrons in 12 orbitals, which includes the C–C σ, σ*; two pairs of σ, σ* from two C–Cu bonds; two pairs of π, π* from two C–O bonds; and two Cu 4*s*-derived orbitals (one occupied and one unoccupied) on the Cu_{16} cluster. The AS for the *O*C–CO adsite was (10e, 10o): C–C σ, σ*, π, π*, O–Cu σ, σ*, C–Cu σ, σ*, and two Cu 4*s*-derived orbitals on the Cu_{10} cluster. The AS for the *CO–*COH adsite was (12e, 12o): C–C σ, σ*, three pairs of σ, σ* from three C–Cu bonds, C–O π, π*, and two Cu 4*s*-derived orbitals and electrons on the Cu_{11} cluster. The AS for the *CO–CHO adsite was (12e, 12o): C–C σ, σ*, C–Cu σ, σ*, two pairs of π, π* from two C–O bonds, and four Cu 4*s*-derived orbitals and electrons on the Cu_{11} cluster. The AS for the *COH–*COH adsite was (12e, 12o): C–C σ, σ*, π, π*, two pairs of σ, σ* from two C–Cu bonds, and four Cu 4*s*-derived orbitals and electrons on the Cu_{10} cluster. The AS for the *OCH–*OCH adsite was (14e, 14o): C–C σ, σ*, π, π*, two pairs of σ, σ* from two O–Cu bonds, four O 2*p* lone-pair electrons (one lone pair on each O) and their correlating virtual orbitals, and two Cu 4*s*-derived orbitals and electrons on the Cu_{10} cluster. The AS for the *COH–CHO adsite was (10e, 10o): C–C σ, σ*, two pairs of σ, σ* from two C–Cu bonds, C–O π, π*, and two Cu 4*s*-derived orbitals and electrons on the Cu_{10} cluster.

We selected larger or at least equal size emb-CASSCF ASs for studying reaction pathways versus screening for adsites for the products to account for the static correlation involved in bond breaking and forming along the paths, especially at transition states. We report the ASs of paths (vide infra) based on orbitals and electrons that need to be included for the reactants. The emb-CASSCF AS used to study the *CO–*CO and *O*C–CO paths was (18e, 14o): the occupied σ_{2s}, σ_{2s}^* formed by C 2*s* and O 2*s* electrons and the two pairs of π, π* from each *CO, and two Cu 4*s*-derived orbitals and electrons on the Cu_{16} or Cu_{10} cluster. The AS for the *CO–*COH path was (16e, 14o): the occupied σ_{2s}, σ_{2s}^* and the two pairs of π, π* from *CO; three pairs of C–Cu σ, σ* from *COH; and two Cu 4*s*-derived orbitals and electrons on the Cu_{11} cluster. The AS for the *CO–CHO path was (16e, 14o): the occupied σ_{2s}, σ_{2s}^* and the two pairs of π, π* from *CO, C–Cu σ, σ* and C–O σ, σ*, π, π* from *CHO, and two Cu 4*s*-derived orbitals and electrons on the Cu_{11} cluster. The AS for the *COH–*COH path was (12e, 12o): three pairs of C–Cu σ, σ* from each *COH on the Cu_{12} cluster. The AS for the *OCH–*OCH path was (14e, 14o): C–O σ, σ*, π, π* and C–Cu σ, σ* from each *CHO, and two Cu 4*s*-derived orbitals and electrons on the Cu_{12} cluster. The AS for the *COH–CHO path was (14e, 14o): C–O σ, σ*, π, π* and C–Cu σ, σ* from *CHO, three pairs of C–Cu σ, σ* from *COH, and two Cu 4*s*-derived orbitals and electrons on the Cu_{12} cluster.

After generating emb-CASSCF wavefunctions, we include all single and double excitations from all occupied orbitals to all virtual orbitals from all CASSCF reference configurations perturbatively (excluding the core 1s, 2s, and 2p orbitals and electrons of each Cu atom that are subsumed into its ECP, as well as all possible excitations within the AS, which are already included explicitly in the CASSCF) in the subsequent emb-CASPT2 calculations to recover dynamic correlation. We showed previously the necessity to include perturbatively correlation from the semicore 3s and 3p states of Cu to predict more accurately H_2 associative desorption from and CH_4 dissociative adsorption on Cu(111) (76), hence their inclusion here. We applied an ionization potential electron affinity (77) shift of 0.25 hartree to avoid the intruder state problem and a level shift (78) of 0.3 hartree to aid convergence in emb-CASPT2 calculations.

Results and Discussion

Screening All Possible Adsites for C–C Coupling Intermediates within ECW Theory. Two configurations for *CO dimer on the Cu(111) surfaces are possible: 1) both C atoms are bound to the surface (denoted as *CO–*CO; Fig. 1) or 2) the C and the O atoms of only one of the *COs are bound to the surface, i.e., one of the C–O bonds lies parallel to the surface (denoted as *O*C–CO; Fig. 1). Previously, Montoya et al. predicted using DFT with RPBE (18) XC that the *CO–*CO configuration is stable only in the presence of a protonated explicit water layer, while the other configuration, *O*C–CO, is stable in the absence of such a layer, on both Cu(111) and Cu(100) surfaces (79). Xiao et al. found using DFT-PBE that adding two explicit water molecules stabilizes the *CO–*CO configuration via hydrogen bonding to the oxygen atoms (vide infra) on Cu(111) (80). We confirmed that *CO–*CO spontaneously dissociates to two *COs without the two explicit solvating water molecules. Therefore, we incorporated two explicit water molecules in the model to screen for stable *CO–*CO adsites and in the determination of the MEP of the *CO–*CO pathway. In this initial adsite screening, no explicit water molecules were added in the study of other C–C coupling paths because no other coupling products spontaneously dissociate.

For most of the intermediates (*CO–*CO, *O*C–CO, *CO–*COH, *COH–*COH, and *OCH–*OCH) studied here, two atoms are covalently bound to the Cu surface, leading to more possible adsites for the dimers than what has been investigated previously for C_1 adsorbates (44, 45). The various possible combinations of C_1 adsorbates (*CO, *COH, and *CHO) considered also compound the complexity. We first established a protocol to identify all possible adsite structures for each adsorbate optimized at the level of DFT-PBE-D3 (details in *SI Appendix*, Note S1). *SI Appendix*, Fig. S22 and Table S1 show the identified stable or metastable geometries and their relative stability, respectively. We then performed emb-CASPT2 calculations using the DFT-PBE-D3–predicted geometries to confirm their stability (or metastability). This step of obtaining the emb-CASPT2–preferred adsite for each intermediate remains essential because in the subsequent reaction pathway optimizations at the PW DFT-PBE-D3 level, we constrain the reactant and product structures to be those DFT-PBE-D3 optimized structures at the emb-CASPT2–preferred adsites, in order to enhance the probability that the subsequent DFT-PBE-D3–predicted pathway with end points thus constrained lies closer to what should be the correct set of structures along the MEP. The emb-CASPT2–predicted preferred adsites for C_1 adsorbates, namely, *CO, *COH, and *CHO (the reactants in the C–C coupling pathways), reside on atop, hexagonal-close-packed (hcp) hollow, and bidentate atop sites, respectively, as identified in our previous work (44).

For the seven C–C coupling products, emb-CASPT2 and DFT-PBE-D3 predict the same preferred adsites for *O*C–CO (atop-bridge site is O at atop and C at bridge), *COH–*COH (fcc-hcp site is one C at a face-centered cubic [fcc] hollow and the other C at an hcp hollow), and *COH–CHO (bridge site), shown as final states (FSs) in Fig. 2 *B*, *E*, and *G*, respectively (Table 1). However, the two theories predict different preferred adsites for other C–C coupling intermediates, namely, *CO–*CO (atop-bridge by emb-CASPT2 [FS in Fig. 2*A*] vs. bridge-bridge by DFT-PBE-D3), *CO–*COH (fcc-hcp by emb-CASPT2 [FS in Fig. 2*C*] vs. hcp-fcc by DFT-PBE-D3), *CO–CHO (atop by emb-CASPT2 [FS in Fig. 2*D*] vs. fcc by DFT-PBE-D3), and *OCH–*OCH (fcc-hcp by emb-CASPT2 [FS in Fig. 2*F*] vs. bridge-bridge by DFT-PBE-D3) (Table 1). For those cases where emb-CASPT2 and DFT-PBE-D3 do not agree as to adsite preference, *SI Appendix*, Fig. S22 shows the DFT-PBE-D3–preferred structures. For these cases, if we compare the relative energies of the two preferred adsites, within either DFT-PBE-D3 or emb-CASPT2, we see they differ by ~0.1 eV or less for *CO–*CO, *CO–*COH, and *OCH–*OCH, whereas the difference is ~0.2 eV for *CO–CHO (*SI Appendix*, Table S1), suggesting that multiple adsites may be accessible for at least three of these potential intermediates. Nevertheless, to avoid further complexity, we choose to optimize the MEPs on the basis of the lowest energy structure predicted at the emb-CASPT2 level.

C–C Coupling Pathways Evaluated by ECW Theory. Here we report the energetics predicted by both DFT-PBE-D3 and emb-CASPT2 for the same DFT-PBE-D3–optimized pathway for each C–C formation route, subject to the constraints on reactant and product structures outlined above. We first considered the formation of *CO dimer. Starting from the emb-CASPT2–preferred adsite structures (atop for *CO; atop-bridge for *CO–*CO), we optimized the MEP of the *CO–*CO reaction path at the PW DFT-PBE-D3 level using CI-NEB, yielding an activation free energy of 0.46 eV and a reaction free energy of 0.42 eV (Fig. 3, gray bars as labeled). Initially, the two *COs chemisorb at two adjacent atop sites and then move toward each other, forming a C–C bond that lies parallel to the surface. Finally, the fully formed *CO–*CO resides on an atop-bridge site with the two explicit water molecules solvating the Os (Fig. 2*A*). We then performed ECW theory to correct the energetics at each interpolated structure along the pathway. emb-CASPT2(18e,14o) (see *Computational Methods* for AS) predicts similar energetics as DFT-PBE-D3, only slightly increasing the activation free energy to 0.59 eV and the reaction free energy to 0.49 eV (Fig. 3, orange bars as labeled). Thus, the *CO dimer, while kinetically accessible, is thermodynamically unlikely to form on Cu(111). Moreover, the barrier for *CO–*CO decoupling is sufficiently low (0.04 eV at the DFT-PBE-D3 level and 0.10 eV at the emb-CASPT2 level) that we conclude *CO–*CO on Cu(111) exists at most only transiently. Montoya et al. examined *CO–*CO hydrogenation paths with DFT-RPBE to predict *CO–*CO can hydrogenate to form *CO–CHO via potential-independent surface *H transfer with a barrier of 0.75 eV on Cu(111) (79). Xiao et al. used DFT-PBE and a constant electrochemical potential model to predict instead that *CO–*COH is the more favorable *CO–*CO hydrogenation product on that same facet, also with a sizeable barrier of 0.61 eV at an applied potential of −0.9 V vs. the RHE (the potential at which ethylene starts forming) (80). The much higher barriers for *CO–*CO hydrogenation versus dissociation indicate that *CO–*CO formation will not be a viable C–C coupling pathway on Cu(111). Consistent with our prediction, Schouten et al. previously speculated that a pathway involving *CO dimerization toward ethylene formation might exist only on Cu(100), not on Cu(111), at low cathodic potentials (11). For the other *CO dimerization route forming *O*C–CO, DFT-PBE-D3 predicts much higher activation (1.40 eV) and reaction (1.35 eV) free energies (Fig. 3). Starting from the same reactant structure of two *COs chemisorbing at two emb-CASPT2–preferred atop sites, one *CO bends toward the surface with both C and O atoms bound to the surface, while the other *CO partly desorbs from the surface to approach the C atom in the first CO forming a C–C bond. At the product structure, the fully formed *O*C–CO reorients to the atop-bridge site with one C–O bond lying parallel to the surface and the other C–O bond axis at an angle to the surface (Fig. 2*B*). We then performed emb-CASPT2(18e, 14o) calculations along this pathway where we used the same AS as in the *CO–*CO path. Emb-CASPT2 yields even higher activation (2.25 eV) and reaction (2.19 eV) free energies, suggesting this pathway (and product) is not viable (Fig. 3).

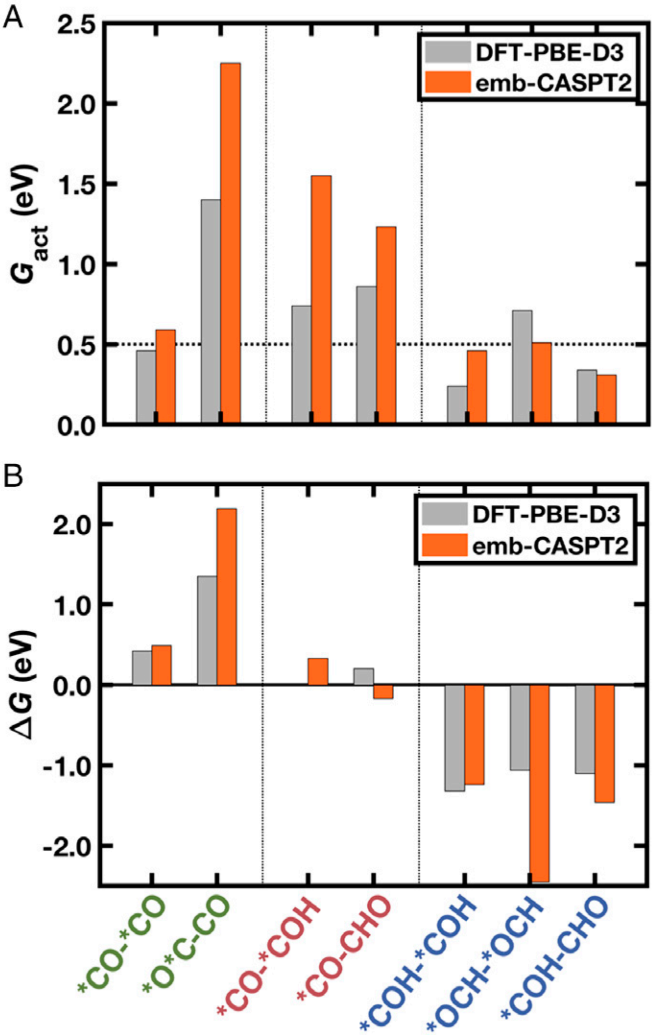

Fig. 3. (*A*) Activation (G_{act}) and (*B*) reaction free energies (ΔG) for C–C coupling paths on Cu(111) predicted by DFT-PBE-D3 (gray bars) and emb-CASPT2 (orange bars). The C–C coupling steps are nonelectroactive; therefore, their activation and free energies do not depend on applied potential. The horizontal black dashed line in *A* indicates an easily kinetically accessible activation energy of 0.5 eV at room temperature (~300 K).

Table 1. Preferred adsites of C–C coupling intermediates evaluated by DFT-PBE-D3 and emb-CASPT2 methods on Cu(111)

	*CO–*CO	*O*C–CO	*CO–*COH	*CO–CHO
DFT-PBE-D3	bridge-bridge	atop-bridge	hcp-fcc	fcc
emb-CASPT2	atop-bridge	atop-bridge	fcc-hcp	atop
	*COH–*COH	*OCH-OCH	*COH–CHO	
DFT-PBE-D3	fcc-hcp	bridge-bridge	bridge	
emb-CASPT2	fcc-hcp	fcc-hcp	bridge	

Atomic structures are shown in Fig. 2 *A*–*G* as final states or in *SI Appendix*, Fig. S22.

We next considered C–C coupling through *CO reacting with a hydrogenated *CO species (either *COH or *CHO). We discuss the *CO–*COH pathway first. Starting from the preferred emb-CASPT2 adsite structures (atop for *CO, hcp hollow for *COH, and fcc-hcp for *CO–*COH), DFT-PBE-D3 predicts an activation free energy of 0.74 eV and a reaction free energy of

−0.01 eV (Fig. 3). Initially, the *CO and *COH move toward each other, forming a C–C bond lying parallel to the surface at the transition state; then the formed *CO–*COH intermediate reorients toward the most stable fcc-hcp site at the final state (Fig. 2*C*). emb-CASPT2(16e, 14o) predicts a much higher activation free energy of 1.55 eV and a reaction free energy of 0.33 eV, indicating this pathway is not kinetically accessible (Fig. 3), consistent with the experimental study by Pérez-Gallent et al. in which they did not observe *CO–*COH as an intermediate on Cu(111), although it was detected on Cu(100) (12). For *CO reacting with *CHO to form *CO–CHO, DFT-PBE-D3 predicts a similar activation free energy of 0.86 eV and a slightly higher reaction free energy of 0.20 eV compared with the *CO–*COH pathway (Fig. 3). Initially, *CO and *CHO are constrained to chemisorb at their emb-CASPT2–preferred sites (atop for *CO; bidentate atop for *CHO). At the transition state, the two adsorbates move toward each other to form a C–C bond, with the center of the bond roughly on top of a Cu atom (Fig. 2*D*). Finally, the formed *CO–CHO reorients to the emb-CASPT2–predicted atop site, with the C atom of the initial *CO bound to the surface and the O atom of the initial *CHO forming a dative bond from one of its lone pairs to the surface. Similar to the *CO–*COH pathway, emb-CASPT2(16e, 14o) further increases the activation free energy to 1.23 eV, which will inhibit this C–C coupling pathway, although it predicts a lower reaction free energy of −0.17 eV (Fig. 3).

We then investigated C–C coupling paths via two hydrogenated *CO species (either *COH or *CHO), leading to three possible products (*COH–*COH, *OCH–*OCH, and *COH–CHO). For the *COH–*COH reaction path, DFT-PBE-D3 predicts an activation free energy of 0.24 eV and a reaction free energy of −1.32 eV (Fig. 3), indicating that this process is both kinetically favorable and exoergic. Along this pathway, two *COHs initially adsorbed at hcp-hollow sites approach each other to form a C–C bond. The *COH–*COH product eventually resides on the most stable fcc-hcp site (Fig. 2*E*). Switching to a higher-level theory, we still find this pathway to be kinetically accessible, although emb-CASPT2(12e, 12o) predicts a slightly higher barrier of 0.46 eV and a slightly less negative reaction free energy of −1.24 eV (Fig. 3). For the *OCH–*OCH pathway, the reaction begins with two *CHO. Each *CHO resides initially on top of two adjacent Cu atoms with the C atom covalently bound to one Cu while the O atom forms a dative bond (using its lone pair) to the other Cu atom (Fig. 2*F*). At the transition state, two *CHOs approach to form a C=C bond, where concurrently two C–Cu bonds break as the two O atoms move downward until stronger O–Cu bonds form to yield the final configuration of *OCH–*OCH (Fig. 2*F*). The fully formed C_2 adsorbate, *OCH–*OCH, rests on the surface with one O on an fcc and another O on an adjacent hcp hollow site (fcc-hcp site). The short C=C bond (1.36 Å) lies parallel to the surface with its center on top of a Cu atom (Fig. 2*F*). DFT-PBE-D3 predicts this path to be exoergic with a reaction free energy of −1.06 eV but with a relatively large activation free energy of 0.71 eV (Fig. 3). However, emb-CASPT2(14e, 14o) predicts a lower barrier of 0.51 eV, as well as a much more negative reaction free energy of −2.45 eV, indicating that this process also is kinetically accessible (Fig. 3). The large exoergicity of this reaction is unsurprising, given that a very strong C=C double bond and polar covalent Cu–O bonds form (with the latter bonds collectively likely stronger than the two original Cu–C bonds in *CHO), yielding a potential immediate precursor to ethylene.

Last, we considered the *COH–CHO pathway that utilizes two different C_1 adsorbates: one *COH and one *CHO. To the best of our knowledge, no previous study has proposed this pathway. Our prior work (45) in which we predicted from ECW theory that both *COH and *CHO may coexist on Cu(111) at experimental onset potentials motivates examination of this alternative C–C coupling pathway. Starting from the emb-CASPT2–preferred adsites for the C_1 precursors (hcp hollow for *COH and bidentate atop for *CHO), a bridge site bound *COH–CHO forms (Fig. 2*G*). Along this pathway, the *COH migrates from an hcp to an fcc hollow site as it approaches the *CHO. At the transition state, as the C–C bond forms, the original C–Cu bond between the *CHO and the surface breaks. Finally, the transition state pivots toward the most stable configuration where the C atom from the *COH resides at a bridge site with the primary molecular plane bisecting the bridge site. The terminal carbonyl O also forms a dative bond to a Cu atom. DFT-PBE-D3 predicts an easily accessible barrier of 0.34 eV and a reaction free energy of −1.10 eV, indicating an exoergic and kinetically accessible step (Fig. 3). However, our previous DFT-PBE-D3 studies predict that *CHO is not a competitive *CO hydrogenation product on Cu(111), blocking the possibility of forming *COH–CHO (or any *CHO-containing coupling product) on this surface (45). Switching to emb-CASPT2(14e, 14o), it predicts a similar barrier of 0.31 eV but an even more negative reaction free energy of −1.46 eV. Therefore, emb-CASPT2 predicts this reaction to be a favorable C–C coupling step (Fig. 3), and in fact, it is the most kinetically favorable within emb-CASPT2.

Effect of Explicit Water Molecules on the Energetics. In the *CO–*CO model, we included two explicit water molecules to stabilize *CO–*CO via hydrogen bonds between water and the O atoms of *CO (FS in Fig. 2*A*). For the *O*C–CO, *CO–*COH, and *CO–CHO paths, the oxygen atom initially from the *CO in principle also might form a hydrogen bond with an explicit water molecule, perhaps stabilizing those complexes as well. Above we predicted these pathways to be unfavorable for C–C coupling in the absence of coadsorbed water. We therefore examined whether inclusion of explicit water molecules that may hydrogen bond to *CO decreases the barriers for these reactions. We observed only small effects of no more than 0.1 eV on barriers (1.40 vs. 1.30 eV for *O*C–CO, 0.74 vs. 0.70 eV for *CO–*COH, and 0.86 vs. 0.83 eV for *CO–CHO) when including one or two explicit water molecules at the DFT-PBE-D3 level (*SI Appendix*, Fig. S23 and Table S2). We then selected the *CO–CHO pathway with one explicit water molecule on which to perform emb-CASPT2 calculations because the *CO–CHO pathway exhibits the lowest emb-CASPT2 activation free energy among the three abovementioned reactions when no explicit water molecule is present. The activation free energy decreases from 1.23 to 1.07 eV (*SI Appendix*, Table S2), which is still not viable kinetically at room temperature. Assuming that each hydrogen-bonded water molecule reduced the barrier by 0.15 eV, we can expect insufficiently large reductions in the respective emb-CASPT2 activation free energies of the other two reactions (2.25 and 1.55 eV for *O*C–CO and *CO–*COH, respectively; Fig. 3*A* and *SI Appendix*, Table S2) to enable those pathways to participate. For completeness, we also examined the effect of including two explicit water molecules on the energetics for C–C coupling pathways via two hydrogenated *CO species. We again find that the presence of explicit waters has only a slight influence on the barriers (0.24 vs. 0.17 eV for *COH–*COH, 0.71 vs. 0.84 eV for *OCH–*OCH, and 0.34 vs. 0.27 eV for

*COH–CHO) at the DFT-PBE-D3 level (*SI Appendix*, Fig. S23 and Table S2). Therefore, even when further accounting for solvation, our conclusions remain the same.

Previously, Monteiro et al. showed that cations (specifically large, polarizable, monovalent cations) enhance electrochemical CO_2 reduction on Cu, Ag, and Au electrodes by stabilizing an adsorbed negatively charged bent CO_2 (81), with acidic cations favoring CO_2R over the hydrogen evolution reaction at low overpotentials and low pH (82). Pérez-Gallent et al. observed that larger cations increase selectivity toward ethylene at low overpotentials and improve yield of methane production at high overpotentials. However, cations have negligible effect on the onset potentials for either ethylene or methane formation (83). Other theoretical studies have explored cation effects on activity (84) and binding energies of key intermediates in CO_2R (85). However, the full reaction mechanism of CO_2R including cation effects has yet to be determined. One other probable role of cations may be to stabilize C_2 products containing a CO functional group, akin to the role of solvating water (vide supra). To simulate this process properly, one would have to identify the proper number of explicit water molecules to solvate the cation, the counter anion and its solvation shell, and the concentration of the ions near the surface (of which cell size may control). How such cations affect these reactions is left for future work.

Most Important C_1 Precursors. Overall, emb-CASPT2 predicts that spontaneous C–C bond formation (exoergic reaction) requires two adsorbed hydrogenated CO species, either *COH or *CHO, resulting in three kinetically feasible pathways with barriers lower than or around 0.5 eV, namely, the *COH–CHO, *COH–*COH, and *OCH–*OCH paths. Among them, the proposed *COH–CHO path is the most kinetically favorable. In contrast, DFT-PBE-D3 predicts that C–C coupling can be realized through the *COH–*COH and *CO–*CO pathways with a preference for the *COH–*COH path. These results raise the question, is there a singularly important precursor for generating C_2 products? Certainly, the coexistence of *COH and *CHO enables fast and favorable C–C bond formation. The role of *CO remains less critical for coupling. We recently predicted that *CO reduces almost equally to *CHO and *COH at an experimental applied potential of −0.9 V vs. the RHE with surmountable barriers of ~0.6 eV on Cu(111) using emb-CASPT2 (45), suggesting coexistence of *COH and *CHO. We also verified that these species can stably coexist on Cu(111) up to at least 0.5 monolayers (*SI Appendix*, Note S2 and Fig. S24). Coexistence of the two species will enable heterocoupling to produce *COH–CHO—the most kinetically accessible coupling product—on this facet. Both *CHO and/or *COH also may be important precursors to C_1 products, including methane. Therefore, comparing the barrier of *CHO and *COH hydrogenation toward C_1 products with the barrier of the most favorable C–C coupling pathway (*COH–CHO formation) toward C_2 products will be essential to understanding the observed high selectivity toward methane on pristine Cu(111). We are currently exploring via ECW theory the entire reaction mechanism for electrochemical CO reduction to methane on Cu(111) to gain further insight into the observed selectivity of Cu(111) for C_1 over C_2 products. Last, because the emb-CASPT2–predicted barriers for CO reduction to either *CHO or *COH at an experimental applied potential of −0.9 V vs. the RHE are higher (~0.6 eV) (45) than the barriers of the most kinetically favorable C–C coupling steps, CO reduction might be the rate-determining step for generating C_2 products on Cu(111). This finding indicates that the second hydrogenation step of these C_1 intermediates is crucial in tuning Cu(111)'s C_1 vs. C_2 selectivity. Indeed, a recent experimental study by Chang et al. is consistent with this conclusion, by providing evidence that the rate-determining step in the formation of C_2 products on Cu is unlikely to be the C–C coupling itself, but instead, hydrogenation of CO likely controls the kinetics (86). Moreover, this finding of the hydrogenation step being more critical than the C–C coupling step for C_2 product formation explains the observation by Schouten et al. that ethylene formation is pH dependent on Cu(111) (11). In contrast, these same authors found on Cu(100) that ethylene formation at low overpotentials (potentials at which methane does not yet form) is pH-independent; they therefore concluded that C–C coupling is the rate-determining step and suggested that *CO dimerization is a viable pathway to form ethylene (11). We currently are verifying this hypothesis by exploring reaction mechanisms for CO hydrogenation and C–C coupling on other facets within ECW theory, to deepen understanding of facet influence on CO_2R selectivity.

Understanding Different Energetics Predicted by emb-CASPT2 and DFT-PBE-D3. Standard XC functionals in DFT frequently fail to describe charge transfer and bond breaking/forming processes adequately due to its single-determinant representation, electron self-interaction and delocalization error, and lack of energy derivative discontinuity with respect to orbital occupation (87). One therefore can assume that the quantitative inaccuracy of DFT-PBE-D3 energetics may be correlated to its incorrect description of charge transfer/delocalization/polarization, i.e., charge evolution as the reactant transforms into the transition (product) state, which correspondingly affects the activation (reaction) free energy. To verify this assumption, we calculated the differences in predicted overall charge changes on the adsorbates (reactant state to transition state, $\Delta q_{\text{TS-R}}$; reactant state to product state, $\Delta q_{\text{P-R}}$) using Bader charge analysis (88, 89), comparing the emb-CASSCF versus emb-DFT-PBE electron densities for the seven C–C coupling steps studied here (*SI Appendix*, Table S3). We used the electron densities from the emb-DFT-PBE cluster model instead of from the DFT-PBE-D3 slab model, to approximate changes in the partitioned electron charge on the adsorbates at the DFT-PBE level for consistency in basis set when comparing CASSCF and DFT-PBE Bader charges. We observed a considerable correlation ($R^2 = 0.67$) between energy differences predicted by emb-CASPT2 versus DFT-PBE-D3 and differences in the predicted change in electron charge on the adsorbates using emb-CASSCF versus emb-DFT-PBE cluster electron densities for both activation and reaction free energies (Fig. 4). These results verify our assumption that the quantitative inaccuracy of energetics predicted by DFT-PBE-D3 comes in part from its inaccurate description of charge transfer processes.

Conclusions

Our recent reevaluation of a key CO_2R step on Cu(111), CO reduction via PCET, revealed that ECW theory yields predictions quantitatively more consistent with experiment than those from conventional DFT (45). Those ECW predictions further asserted coexistence of *COH and *CHO intermediates on Cu(111) at experimental onset potentials, unlike conventional DFT that exhibits a strong preference for *COH (45). Thus, in the present work, we employed this same high-level theory to reexamine

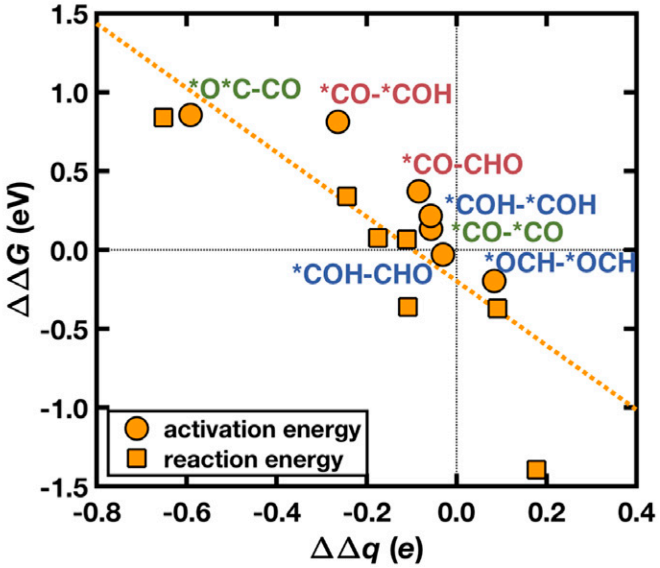

Fig. 4. Plot of the predicted free energy difference between emb-CASPT2 and DFT-PBE-D3 (ΔΔ*G*) versus adsorbate charge change difference between emb-CASSCF and emb-DFT-PBE cluster models (ΔΔ*q*) for the seven C–C coupling activation (circles) and reaction (squares) free energies. Bader charge changes of adsorbates between transition (product) and reactant states are used to correlate with activation (reaction) free energies. Only the data corresponding to the activation free energy differences are labeled.

various C–C coupling steps on Cu(111) on the path toward C_2 products, including both of these intermediates as reactants. We first determined stable adsites of each possible C–C coupling intermediate with ECW theory and noted disagreement between DFT-PBE-D3– and emb-CASPT2–predicted adsites for four C_2 adsorbates (*CO–*CO, *CO–*COH, *CO–CHO, and *OCH–*OCH), indicating the necessity of applying this more rigorous theory to evaluate, even qualitatively, CO_2RR mechanisms. Starting from these ECW-predicted adsites, we optimized all possible C–C coupling pathways (formed by any combination of two C_1 precursors, namely, *CO, *COH, and *CHO) at the DFT-PBE-D3 level of theory and then corrected the energetics along MEPs with emb-CASPT2. DFT-PBE-D3 finds two kinetically feasible C–C coupling steps on Cu(111) with activation barriers less than 0.5 eV, including *COH–*COH (0.24 eV) and *CO–*CO (0.46 eV) pathways. By contrast, emb-CASPT2 predicts that C–C coupling on Cu(111) occurs most favorably through the heterogeneous coupling of one *COH precursor with one *CHO precursor (*COH–CHO) with a barrier of 0.31 eV. The two other, homogeneous coupling pathways are only slightly less favorable: two *COH species (*COH–*COH) couple with a barrier of 0.46 eV or two *CHO species couple (*OCH–*OCH) with a barrier of 0.51 eV. The *COH–CHO path dominates, which was overlooked previously because prior modeling with only DFT approximations proposed either *CHO or *COH intermediates, but not both, as a CO reduction product, depending on the Cu facet. These proposed mechanisms inspire a design principle for CO_2R electrocatalysts: enabling coexistence and dominance of both hydrogenated CO species (*COH and *CHO) could accelerate and strengthen preference for C–C bond formation and thus improve activity and selectivity toward multicarbon products. This work once again demonstrates the importance of applying a qualitatively and quantitatively reliable quantum mechanical method to study electrochemistry, elucidate the CO_2RR mechanism toward more reduced C_2 products, and ultimately shed light on ways to enhance CO_2R activity and selectivity via electrocatalysis.

Data, Materials, and Software Availability. All study data are included in the article and/or supporting information. The embedding subroutine (extpot.F) that is not packaged with the standard VASP code and associated Python scripts, and the standalone embedding integral generator code used to transform the embedding potential from a Cartesian grid to atomic orbital (GTO) bases, are available via GitHub: https://github.com/EACcodes/VASPEmbedding (90) and https://github.com/EACcodes/EmbeddingIntegralGenerator (91), respectively, both under the Mozilla Public License 2.0.

ACKNOWLEDGMENTS. This work was supported as part of the Advanced Scientific Computing Research Program funded by the US Department of Energy, Office of Science, Basic Energy Sciences, under Award DE-AC02-05CH11231. This work was carried out using computational resources from Princeton University's Terascale Infrastructure for Groundbreaking Research in Engineering and Science. We thank Ms. Samantha Luu for providing a critical reading and careful editing of the manuscript.

Author affiliations: [a]Department of Mechanical and Aerospace Engineering, Princeton University, Princeton, NJ 08544-5263; [b]Department of Chemical and Biomolecular Engineering, University of California, Los Angeles, CA 90095-1592; and [c]Andlinger Center for Energy and the Environment, Princeton University, Princeton, NJ 08544-5263

1. S. Xu, E. A. Carter, Theoretical insights into heterogeneous (photo)electrochemical CO_2 reduction. *Chem. Rev.* **119**, 6631–6669 (2019).
2. S. Nitopi *et al.*, Progress and perspectives of electrochemical CO_2 reduction on copper in aqueous electrolyte. *Chem. Rev.* **119**, 7610–7672 (2019).
3. Y. Y. Birdja *et al.*, Advances and challenges in understanding the electrocatalytic conversion of carbon dioxide to fuels. *Nat. Energy* **4**, 732–745 (2019).
4. M. G. Kibria *et al.*, Electrochemical CO_2 reduction into chemical feedstocks: From mechanistic electrocatalysis models to system design. *Adv. Mater.* **31**, e1807166 (2019).
5. Y. Hori, K. Kikuchi, S. Suzuki, Production of CO and CH_4 in electrochemical reduction of CO_2 at metal electrodes in aqueous hydrogencarbonate solution. *Chem. Lett.* **14**, 1695–1698 (1985).
6. Y. Hori, H. Wakebe, T. Tsukamoto, O. Koga, Electrocatalytic process of CO selectivity in electrochemical reduction of CO_2 at metal electrodes in aqueous media. *Electrochim. Acta* **39**, 1833–1839 (1994).
7. Y. Hori, "Electrochemical CO2 reduction on metal electrodes" in *Modern Aspects of Electrochemistry*, C. G. Vayenas, R. E. White, M. E. Gamboa-Aldeco, Eds. (Springer, 2008), pp. 89–189.
8. R. Kortlever, J. Shen, K. J. P. Schouten, F. Calle-Vallejo, M. T. M. Koper, Catalysts and reaction pathways for the electrochemical reduction of carbon dioxide. *J. Phys. Chem. Lett.* **6**, 4073–4082 (2015).
9. M. Zhong *et al.*, Accelerated discovery of CO_2 electrocatalysts using active machine learning. *Nature* **581**, 178–183 (2020).
10. K. P. Kuhl, E. R. Cave, D. N. Abram, T. F. Jaramillo, New insights into the electrochemical reduction of carbon dioxide on metallic copper surfaces. *Energy Environ. Sci.* **5**, 7050–7059 (2012).
11. K. J. P. Schouten, Z. Qin, E. Pérez Gallent, M. T. M. Koper, Two pathways for the formation of ethylene in CO reduction on single-crystal copper electrodes. *J. Am. Chem. Soc.* **134**, 9864–9867 (2012).
12. E. Pérez-Gallent, M. C. Figueiredo, F. Calle-Vallejo, M. T. M. Koper, Spectroscopic observation of a hydrogenated CO dimer intermediate during CO reduction on Cu(100) electrodes. *Angew. Chem. Int. Ed. Engl.* **56**, 3621–3624 (2017).
13. K. J. P. Schouten, E. Pérez-Gallent, M. T. M. Koper, The influence of pH on the reduction of CO and CO_2 to hydrocarbons on copper electrodes. *J. Electroanal. Chem.* **716**, 53–57 (2014).
14. K. J. P. Schouten, Y. Kwon, C. J. M. Van der Ham, Z. Qin, M. T. M. Koper, A new mechanism for the selectivity to C_1 and C_2 species in the electrochemical reduction of carbon dioxide on copper electrodes. *Chem. Sci.* **2**, 1902–1909 (2011).
15. E. Bertheussen *et al.*, Acetaldehyde as an intermediate in the electroreduction of carbon monoxide to ethanol on oxide-derived copper. *Angew. Chem. Int. Ed. Engl.* **55**, 1450–1454 (2016).
16. J. P. Perdew, K. Burke, M. Ernzerhof, Generalized gradient approximation made simple. *Phys. Rev. Lett.* **77**, 3865–3868 (1996).
17. W. Luo, X. Nie, M. J. Janik, A. Asthagiri, Facet dependence of CO_2 reduction paths on Cu electrodes. *ACS Catal.* **6**, 219–229 (2016).
18. B. Hammer, L. B. Hansen, J. K. Nørskov, Improved adsorption energetics within density-functional theory using revised Perdew-Burke-Ernzerhof functionals. *Phys. Rev. B Condens. Matter Mater. Phys.* **59**, 7413 (1999).
19. A. J. Garza, A. T. Bell, M. Head-Gordon, Mechanism of CO_2 reduction at copper surfaces: Pathways to C_2 products. *ACS Catal.* **8**, 1490–1499 (2018).
20. F. Calle-Vallejo, M. T. M. Koper, Theoretical considerations on the electroreduction of CO to C_2 species on Cu(100) electrodes. *Angew. Chem. Int. Ed. Engl.* **52**, 7282–7285 (2013).
21. T. Cheng, H. Xiao, W. A. Goddard, 3rd, Full atomistic reaction mechanism with kinetics for CO reduction on Cu(100) from ab initio molecular dynamics free-energy calculations at 298 K. *Proc. Natl. Acad. Sci. U.S.A.* **114**, 1795–1800 (2017).
22. J. Wellendorff *et al.*, Density functionals for surface science: Exchange-correlation model development with Bayesian error estimation. *Phys. Rev. B Condens. Matter Mater. Phys.* **85**, 235149 (2012).
23. X. Liu *et al.*, pH effects on the electrochemical reduction of $CO_{(2)}$ towards C_2 products on stepped copper. *Nat. Commun.* **10**, 32 (2019).

24. H. Xiao, T. Cheng, W. A. Goddard, 3rd, Atomistic mechanisms underlying selectivities in C_1 and C_2 products from electrochemical reduction of CO on Cu(111). *J. Am. Chem. Soc.* **139**, 130–136 (2017).
25. K. Chan, A few basic concepts in electrochemical carbon dioxide reduction. *Nat. Commun.* **11**, 5954 (2020).
26. H. H. Kristoffersen, K. Chan, Towards constant potential modeling of CO-CO coupling at liquid water-Cu(100) interfaces. *J. Catal.* **396**, 251–260 (2021).
27. N. Govindarajan, A. Xu, K. Chan, How pH affects electrochemical processes. *Science* **375**, 379–380 (2022).
28. L. D. Chen, M. Urushihara, K. Chan, J. K. Nørskov, Electric field effects in electrochemical CO_2 reduction. *ACS Catal.* **6**, 7133–7139 (2016).
29. M. Neef, K. Doll, CO adsorption on the Cu(111) surface: A density functional study. *Surf. Sci.* **600**, 1085–1092 (2006).
30. S. Luo, Y. Zhao, D. G. Truhlar, Improved CO adsorption energies, site preferences, and surface formation energies from a meta-generalized gradient approximation exchange–correlation functional, M06-L. *J. Phys. Chem. Lett.* **3**, 2975–2979 (2012).
31. J. Wellendorff *et al.*, A benchmark database for adsorption bond energies to transition metal surfaces and comparison to selected DFT functionals. *Surf. Sci.* **640**, 36–44 (2015).
32. S. M. Sharada, T. Bligaard, A. C. Luntz, G.-J. Kroes, J. K. Nørskov, SBH10: A benchmark database of barrier heights on transition metal surfaces. *J. Phys. Chem. C* **121**, 19807–19815 (2017).
33. Q. Zhao, H. J. Kulik, Stable surfaces that bind too tightly: Can range-separated hybrids or DFT+U improve paradoxical descriptions of surface chemistry? *J. Phys. Chem. Lett.* **10**, 5090–5098 (2019).
34. P. Hollins, J. Pritchard, Interactions of CO molecules adsorbed on Cu(111). *Surf. Sci.* **89**, 486–495 (1979).
35. W. Kirstein, B. Krüger, F. Thieme, CO adsorption studies on pure and Ni-covered Cu(111) surfaces. *Surf. Sci.* **176**, 505–529 (1986).
36. L. Bartels, G. Meyer, K.-H. Rieder, The evolution of CO adsorption on Cu(111) as studied with bare and CO-functionalized scanning tunneling tips. *Surf. Sci.* **432**, L621–L626 (1999).
37. S. Vollmer, G. Witte, C. Wöll, Determination of site specific adsorption energies of CO on copper. *Catal. Lett.* **77**, 97–101 (2001).
38. P. Huang, E. A. Carter, Advances in correlated electronic structure methods for solids, surfaces, and nanostructures. *Annu. Rev. Phys. Chem.* **59**, 261–290 (2008).
39. C. Huang, M. Pavone, E. A. Carter, Quantum mechanical embedding theory based on a unique embedding potential. *J. Chem. Phys.* **134**, 154110 (2011).
40. F. Libisch, C. Huang, E. A. Carter, Embedded correlated wavefunction schemes: Theory and applications. *Acc. Chem. Res.* **47**, 2768–2775 (2014).
41. K. Yu, F. Libisch, E. A. Carter, Implementation of density functional embedding theory within the projector-augmented-wave method and applications to semiconductor defect states. *J. Chem. Phys.* **143**, 102806 (2015).
42. K. Yu, C. M. Krauter, J. M. Dieterich, E. A. Carter, “Density and potential functional embedding: Theory and practice” in *Fragmentation: Toward Accurate Calculations on Complex Molecular Systems*, M. S. Gordon, Ed. (John Wiley & Sons, 2017), pp. 81–118.
43. S. Sharifzadeh, P. Huang, E. A. Carter, Embedded configuration interaction description of CO on Cu(111): Resolution of the site preference conundrum. *J. Phys. Chem. C* **112**, 4649–4657 (2008).
44. Q. Zhao, E. A. Carter, Revisiting competing paths in electrochemical CO_2 reduction on copper via embedded correlated wavefunction theory. *J. Chem. Theory Comput.* **16**, 6528–6538 (2020).
45. Q. Zhao, J. M. P. Martirez, E. A. Carter, Revisiting understanding of electrochemical CO_2 reduction on Cu(111): Competing proton-coupled electron transfer reaction mechanisms revealed by embedded correlated wavefunction theory. *J. Am. Chem. Soc.* **143**, 6152–6164 (2021).
46. O. J. Wahab, M. Kang, E. Daviddi, M. Walker, P. R. Unwin, Screening surface structure-electrochemical activity relationships of copper electrodes under CO_2 electroreduction conditions. *ACS Catal.* **12**, 6578–6588 (2022).
47. B. Zhang *et al.*, Highly electrocatalytic ethylene production from CO_2 on nanodefective Cu nanosheets. *J. Am. Chem. Soc.* **142**, 13606–13613 (2020).
48. Z.-Z. Wu *et al.*, Identification of Cu(100)/Cu(111) interfaces as superior active sites for CO dimerization during CO_2 electroreduction. *J. Am. Chem. Soc.* **144**, 259–269 (2022).
49. Y. Zhou *et al.*, Dopant-induced electron localization drives CO_2 reduction to C_2 hydrocarbons. *Nat. Chem.* **10**, 974–980 (2018).
50. J. C. Bui *et al.*, Engineering catalyst–electrolyte microenvironments to optimize the activity and selectivity for the electrochemical reduction of CO_2 on Cu and Ag. *Acc. Chem. Res.* **55**, 484–494 (2022).
51. G. Kresse, J. Furthmüller, Efficiency of ab-initio total energy calculations for metals and semiconductors using a plane-wave basis set. *Comput. Mater. Sci.* **6**, 15–50 (1996).
52. G. Kresse, J. Furthmüller, Efficient iterative schemes for ab initio total-energy calculations using a plane-wave basis set. *Phys. Rev. B Condens. Matter* **54**, 11169–11186 (1996).
53. S. Grimme, J. Antony, S. Ehrlich, H. Krieg, A consistent and accurate ab initio parametrization of density functional dispersion correction (DFT-D) for the 94 elements H-Pu. *J. Chem. Phys.* **132**, 154104 (2010).
54. S. Grimme, S. Ehrlich, L. Goerigk, Effect of the damping function in dispersion corrected density functional theory. *J. Comput. Chem.* **32**, 1456–1465 (2011).
55. A. D. Becke, E. R. Johnson, A density-functional model of the dispersion interaction. *J. Chem. Phys.* **123**, 154101 (2005).
56. P. E. Blöchl, Projector augmented-wave method. *Phys. Rev. B Condens. Matter* **50**, 17953–17979 (1994).
57. G. Kresse, J. Hafner, Norm-conserving and ultrasoft pseudopotentials for first-row and transition elements. *J. Phys. Condens. Matter* **6**, 8245 (1994).
58. G. Kresse, D. Joubert, From ultrasoft pseudopotentials to the projector augmented-wave method. *Phys. Rev. B Condens. Matter Mater. Phys.* **59**, 1758 (1999).
59. H. J. Monkhorst, J. D. Pack, Special points for Brillouin-zone integrations. *Phys. Rev. B* **13**, 5188 (1976).
60. M. Methfessel, A. T. Paxton, High-precision sampling for Brillouin-zone integration in metals. *Phys. Rev. B Condens. Matter* **40**, 3616–3621 (1989).
61. G. Makov, M. C. Payne, Periodic boundary conditions in ab initio calculations. *Phys. Rev. B Condens. Matter* **51**, 4014–4022 (1995).
62. G. Henkelman, B. P. Uberuaga, H. Jónsson, A climbing image nudged elastic band method for finding saddle points and minimum energy paths. *J. Chem. Phys.* **113**, 9901 (2000).
63. K. Mathew, R. Sundararaman, K. Letchworth-Weaver, T. A. Arias, R. G. Hennig, Implicit solvation model for density-functional study of nanocrystal surfaces and reaction pathways. *J. Chem. Phys.* **140**, 084106 (2014).
64. K. Mathew, V. S. C. Kolluru, S. Mula, S. N. Steinmann, R. G. Hennig, Implicit self-consistent electrolyte model in plane-wave density-functional theory. *J. Chem. Phys.* **151**, 234101 (2019).
65. F. Libisch, C. Huang, P. Liao, M. Pavone, E. A. Carter, Origin of the energy barrier to chemical reactions of O_2 on Al(111): Evidence for charge transfer, not spin selection. *Phys. Rev. Lett.* **109**, 198303 (2012).
66. Q. Wu, W. Yang, A direct optimization method for calculating density functionals and exchange–correlation potentials from electron densities. *J. Chem. Phys.* **118**, 2498 (2003).
67. H.-J. Werner *et al.*, MOLPRO, a package of ab initio programs, version 2015.1. https://www.molpro.net/. Accessed 1 October 2021.
68. H.-J. Werner, P. J. Knowles, G. Knizia, F. R. Manby, M. Schütz, Molpro: A general-purpose quantum chemistry program package. *Wiley Interdiscip. Rev. Comput. Mol. Sci.* **2**, 242–253 (2012).
69. T. H. Dunning Jr., Gaussian basis sets for use in correlated molecular calculations. I. The atoms boron through neon and hydrogen. *J. Chem. Phys.* **90**, 1007 (1989).
70. P. J. Hay, W. R. Wadt, Ab initio effective core potentials for molecular calculations. Potentials for K to Au including the outermost core orbitals. *J. Chem. Phys.* **82**, 299 (1985).
71. C. M. Krauter, E. A. Carter, EmbeddingIntegralGenerator. https://github.com/EACcodes/EmbeddingIntegralGenerator/. Accessed 1 October 2021.
72. K. Andersson, P. A. Malmqvist, B. O. Roos, A. J. Sadlej, K. Wolinski, Second-order perturbation theory with a CASSCF reference function. *J. Phys. Chem.* **94**, 5483–5488 (1990).
73. P. Celani, H.-J. Werner, Multireference perturbation theory for large restricted and selected active space reference wave functions. *J. Chem. Phys.* **112**, 5546 (2000).
74. B. O. Roos, The complete active space SCF method in a fock-matrix-based super-CI formulation. *Int. J. Quantum Chem.* **18**, 175–189 (1980).
75. P. E. M. Siegbahn, J. Almlöf, A. Heiberg, B. O. Roos, The complete active space SCF (CASSCF) method in a Newton–Raphson formulation with application to the HNO molecule. *J. Chem. Phys.* **74**, 2384 (1981).
76. Q. Zhao, X. Zhang, J. M. P. Martirez, E. A. Carter, Benchmarking an embedded adaptive sampling configuration interaction method for surface reactions: H_2 desorption from and CH_4 dissociation on Cu(111). *J. Chem. Theory Comput.* **16**, 7078–7088 (2020).
77. G. Ghigo, B. O. Roos, P.-Å. Malmqvist, A modified definition of the zeroth-order Hamiltonian in multiconfigurational perturbation theory (CASPT2). *Chem. Phys. Lett.* **396**, 142–149 (2004).
78. B. O. Roos, K. Andersson, Multiconfigurational perturbation theory with level shift—The Cr_2 potential revisited. *Chem. Phys. Lett.* **245**, 215–223 (1995).
79. J. H. Montoya, C. Shi, K. Chan, J. K. Nørskov, Theoretical insights into a CO dimerization mechanism in CO_2 electroreduction. *J. Phys. Chem. Lett.* **6**, 2032–2037 (2015).
80. H. Xiao, T. Cheng, W. A. Goddard 3rd, R. Sundararaman, Mechanistic explanation of the pH dependence and onset potentials for hydrocarbon products from electrochemical reduction of CO on Cu(111). *J. Am. Chem. Soc.* **138**, 483–486 (2016).
81. M. C. Monteiro *et al.*, Absence of CO_2 electroreduction on copper, gold and silver electrodes without metal cations in solution. *Nat. Catal.* **4**, 654–662 (2021).
82. M. C. O. Monteiro, F. Dattila, N. López, M. T. M. Koper, The role of cation acidity on the competition between hydrogen evolution and CO_2 reduction on gold electrodes. *J. Am. Chem. Soc.* **144**, 1589–1602 (2022).
83. E. Pérez-Gallent, G. Marcandalli, M. C. Figueiredo, F. Calle-Vallejo, M. T. M. Koper, Structure- and potential-dependent cation effects on CO reduction at copper single-crystal electrodes. *J. Am. Chem. Soc.* **139**, 16412–16419 (2017).
84. S. Ringe *et al.*, Understanding cation effects in electrochemical CO_2 reduction. *Energy Environ. Sci.* **12**, 3001–3014 (2019).
85. T. Ludwig *et al.*, Atomistic insight into cation effects on binding energies in Cu-catalyzed carbon dioxide reduction. *J. Phys. Chem. C* **124**, 24765–24775 (2020).
86. X. Chang *et al.*, C-C coupling is unlikely to be the rate-determining step in the formation of C_{2+} products in the copper-catalyzed electrochemical reduction of CO. *Angew. Chem. Int. Ed. Engl.* **61**, e202111167 (2022).
87. A. J. Cohen, P. Mori-Sánchez, W. Yang, Insights into current limitations of density functional theory. *Science* **321**, 792–794 (2008).
88. R. F. Bader, A quantum theory of molecular structure and its applications. *Chem. Rev.* **91**, 893–928 (1991).
89. W. Tang, E. Sanville, G. Henkelman, A grid-based Bader analysis algorithm without lattice bias. *J. Phys. Condens. Matter* **21**, 084204 (2009).
90. K. Yu, F. Libisch, E. A. Carter, EACcodes / VASPEmbedding. GitHub. https://github.com/EACcodes/VASPEmbedding. Deposited 28 April 2018.
91. C. Krauter, X. Zhang, E. A. Carter, EACcodes / EmbeddingIntegralGenerator. GitHub. https://github.com/EACcodes/EmbeddingIntegralGenerator. Deposited 5 May 2021.